Improved Limit on the Effective Electron Neutrino Mass with the ECHo-1k Experiment

F. Adam,[1,2] F. Ahrens,[3,*] L. E. Ardila Perez,[4] M. Balzer,[4] A. Barth,[3] D. Behrend-Uriarte,[3] S. Berndt,[5,6] K. Blaum,[7] F. W. H. Böhm,[3] M. Braß,[8] L. Calza,[3] K. Chrysalidis,[9] M. Door,[7,†] H. Dorrer,[5] Ch. E. Düllmann,[5,10,11] K. Eberhardt,[5,10] S. Eliseev,[7] C. Enss,[3,4] P. Filianin,[7] A. Fleischmann,[3] R. Gartmann,[4] L. Gastaldo,[3,‡] M. Griedel,[3,§] A. Göggelmann,[12] R. Hammann,[3,∥] R. Hasse,[6] M. W. Haverkort,[8] S. Heinze,[8] D. Hengstler,[3] R. Jeske,[3] J. Jochum,[12] K. Johnston,[9] N. Karcher,[4] S. Kempf,[2,4] T. Kieck,[11,10] U. Köster,[13] N. Kovac,[3,¶] N. Kneip,[6] K. Kromer,[7] F. Mantegazzini,[3,*] B. A. Marsh,[9,†] M. Merstorf,[8] T. Muscheid,[4] M. Neidig,[2] Y. N. Novikov,[7] R. Pandey,[3] A. Reifenberger,[3] D. Richter,[3] A. Rischka,[7] S. Rothe,[9] O. Sander,[4] R. X. Schüssler,[7] S. Scholl,[12] Ch. Schweiger,[7] C. Velte,[3] M. Weber,[14] M. Wegner,[4,2] K. Wendt,[6] and T. Wickenhäuser[3]

(ECHo Collaboration)

[1]*Institute for Astroparticle Physics, Karlsruhe Institute of Technology, Karlsruhe, Germany*
[2]*Institute for Micro- and Nanoelectronic Systems, Karlsruhe Institute of Technology, Karlsruhe, Germany*
[3]*Kirchhoff Institute for Physics, Heidelberg University, Heidelberg, Germany*
[4]*Institute for Data Processing and Electronics, Karlsruhe Institute of Technology, Karlsruhe, Germany*
[5]*Department of Chemistry—TRIGA Site, Johannes Gutenberg University Mainz, Mainz, Germany*
[6]*Institute of Physics, Johannes Gutenberg University Mainz, Mainz, Germany*
[7]*Max Planck Institute for Nuclear Physics, Heidelberg, Germany*
[8]*Institute for Theoretical Physics, Heidelberg University, Heidelberg, Germany*
[9]*ISOLDE, CERN, Geneve, Switzerland/France*
[10]*Helmholtz Institute Mainz, Mainz, Germany*
[11]*GSI Helmholtz Centre for Heavy Ion Research GmbH, Darmstadt, Germany*
[12]*Physics Institute, University of Tübingen, Tübingen, Germany*
[13]*Institut Laue-Langevin, Grenoble, France*
[14]*Division V, Karlsruhe Institute of Technology, Karlsruhe, Germany*

(Received 3 September 2025; revised 15 December 2025; accepted 4 February 2026; published 25 March 2026)

The effective electron neutrino mass can be determined by analyzing the end-point region of the ^{163}Ho electron capture spectrum, provided a measurement with high-energy resolution and high statistics using calorimetric techniques. Here, the Electron Capture in ^{163}Ho Collaboration (ECHo) presents an analysis of the most precise ^{163}Ho spectrum currently available, obtained with the ECHo-1k experiment and comprising about 200 million events. A very low background rate of $b_{\rm const} = 9.1(1.3) \times 10^{-6}$ eV/pixel/day was achieved allowing for a reliable analysis of the end-point region. The derived end-point energy $Q = 2862(4)$ eV is in excellent agreement with the one independently determined via Penning-trap mass spectrometry of $Q = 2863.2(6)$ eV [Ch. Schweiger *et al.*, Nat. Phys. **226**, 921 (2024)]. The upper limit of the effective electron neutrino mass is improved by almost a factor of 2 compared to the lowest current value [B. K. Alpert *et al.*, Phys. Rev. Lett. **135**, 141801 (2025)], reaching $m_{\nu_e} < 15$ eV$/c^2$ (90% credible interval).

DOI: 10.1103/lqkb-hylx

*Present address: Fondazione Bruno Kessler (FBK), I-38123 Trento, Italy and INFN- TIFPA, I-38123 Trento, Italy.
†Present address: Laboratoire Kastler Brossel, Sorbonne University, CNRS, ENS-PSL University, Collège de France, Paris, France.
‡Contact author: Gastaldo@kip.uni-heidelberg.de
§Present address: Institute for Quantum Material and Technologies, Karlsruhe Institute of Technology, Germany.
∥Present address: Max Planck Institute for Nuclear Physics, Heidelberg, Germany.
¶Present address: Institute for Astroparticle Physics, Karlsruhe Institute of Technology, Germany.

The determination of the neutrino mass scale will give guidance for extending the present standard model of particle physics [1] and enable precision tests of the ΛCDM cosmological model [2]. Three different observables, which are functions of the neutrino mass eigenvalues m_i, are investigated to set the neutrino mass scale: the sum of the neutrino mass eigenvalues from the analysis of the distribution of matter in the Universe, the effective Majorana mass which can be derived if neutrinoless double beta decay is observed, and the effective electron neutrino mass [3–7]. Under *CPT* invariance, there is no difference between the effective electron neutrino and electron antineutrino mass m_{ν_e} defined as $m^2_{\nu_\mathrm{e}} = \Sigma|U_\mathrm{ei}|^2 m^2_\mathrm{i}$, where U_ei are elements of the Pontecorvo-Maki-Nakagawa-Sakata matrix and m_i the eigenvalues of the neutrino mass eigenstates. The derivation of this quantity by analyzing the shape of beta and electron capture (EC) spectra in the end-point region relies only on energy and momentum conservation. Therefore, no fundamental physics assumptions should prevent this quantity from being determined, provided that experiments can achieve the required accuracy. On the other hand, a cosmological model needs to be assumed to derive the sum of neutrino mass eigenstates from the matter distribution in the Universe and lepton number violation together with light Majorana neutrinos are required for deriving the Majorana mass from the observation of neutrinoless double beta decay. This approach is followed by several collaborations that focus mainly on the beta decay of ^{3}H and EC of ^{163}Ho [7–13]. The lowest upper limit on the effective electron antineutrino mass $m_{\overline{\nu_\mathrm{e}}} < 0.45\ \mathrm{eV}/c^2$ [90% confidence level (CL)] has been achieved by the KATRIN Collaboration with ^{3}H [14], while the best limit on the effective electron neutrino mass $m_{\nu_\mathrm{e}} < 27\ \mathrm{eV}/c^2$ (90% CL) has been achieved by the HOLMES Collaboration [15].

The ECHo Collaboration [12,16] aims at determining the effective electron neutrino mass by studying the EC decay of ^{163}Ho to ^{163}Dy. The maximum energy available for ^{163}Ho decay is $Q = 2863.2(6)$ eV [17]. Thus, electron capture can occur only starting from the third innermost electron shell. This, in turn, implies an extremely small fraction of photonic deexcitations, favoring deexcitation via Auger processes. To improve the sensitivity of the measurement and avoid systematic uncertainties, which occur in experiments with separated radioactive source and detector, the idea of enclosing the ^{163}Ho source in high-energy resolution detectors was proposed in [18] and is adopted in modern experiments [12,13]. The expected spectral shape in this type of measurements is, in first approximation, characterized by several resonances, each corresponding to an excited state in which the ^{163}Dy atom may be left [19]. The main resonances are MI at 2040 eV corresponding to the capture of 3*s* electrons, MII at 1836 eV for $3p_{1/2}$ electrons, and NI at 411 eV for 4*s* electrons. The key technology in ECHo is based on metallic magnetic calorimeters (MMCs) with enclosed ^{163}Ho. MMCs are operated at temperatures below 20 mK and achieve an energy resolution in the eV range [20–23]. For MMCs optimized for the ECHo experiment, the fraction of events with partial energy detection in a region extending up to 50 eV below the EC end-point energy Q is lower than 2×10^{-8}, ensuring 100% detection efficiency in the end-point region [24,25]. The ECHo experiment has so far gone through two R&D phases. In the first one, the possibility of obtaining a high-resolution ^{163}Ho spectrum using MMCs [26] was demonstrated. Although only four MMC pixels with approximately 0.2 Bq ^{163}Ho activity each were used, the ECHo Collaboration set a new limit for the effective electron-neutrino mass $m_{\nu_\mathrm{e}} < 150\ \mathrm{eV}/c^2$ (95% CL) [26], improving upon the previous best upper limit of $225\ \mathrm{eV}/c^2$ (95% CL) [27]. The second phase, known as ECHo-1k, featured an optimized detector design [25] and a new multichannel readout scheme [28]. The ^{163}Ho source was produced by irradiation of ^{162}Er at the Institut Laue-Langevin in Grenoble and an optimized radiochemical separation ensured the required high purity [29]. The ion-implantation procedure was performed at the upgraded RISIKO facility in Mainz [30,31].

This Letter presents the analysis of the ^{163}Ho EC spectrum measured in the ECHo-1k experiment with a total exposure of 4880 pixel × days and an average activity per pixel of 0.7 Bq [25]. The success of the ECHo-1k experiment lays the foundation for the development of future large-scale experiments using ^{163}Ho, with the aim of achieving sensitivity to the effective electron neutrino mass on par with experiments based on ^{3}H and beyond.

For the ECHo-1k phase, a 72-pixel MMC array (36 channels), called the ECHo-1k chip, has been developed [25]. The MMC design is based on the meander-shaped pickup coil geometry. The first-order gradiometric configuration allows for the simultaneous readout of two pixels [21]. The single-pixel design for the ECHo-1k array has been optimized to achieve an energy resolution of $\Delta E_\mathrm{FWHM} < 10$ eV under realistic noise conditions. In Fig. 1, a schematic drawing of an MMC pixel of the ECHo-1k chip is shown. A meander-shaped niobium coil, microfabricated on a silicon substrate, has the dual function of carrying a persistent current, since niobium is superconducting at the operating temperature of MMCs, and to act as a pickup coil. A paramagnetic Ag:Er sensor is placed on top of the niobium structure and is thermally and mechanically connected to an absorber via three gold stems (for better visibility, the sensor and absorber have been drawn only on one of the two sides of the coil). The persistent current in the niobium coil generates a static magnetic field, leading to a temperature-dependent magnetization of the paramagnetic sensor. The absorber exhibits a sandwich structure consisting of two gold layers. The volume of the first gold layer is 180 μm × 180 μm × 5 μm.

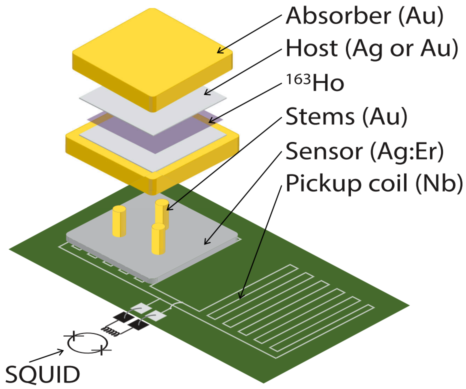

FIG. 1. Schematic drawing of an MMC pixel for the ECHo experiment. For visual clarity, the sensor and absorber are shown for only one of the two pixels, allowing the pickup coil underneath the other to be seen.

Onto the top of this first gold layer, ^{163}Ho ions are implanted within a central area of $150 \times 150\ \mu m^2$ which is covered with a 100 nm thin metallic layer (silver or gold). The implantation energy is 30 keV, corresponding to an average implantation depth of 5 nm [32]. A second gold layer with area $165 \times 165\ \mu m^2$ and thickness of 5 μm is deposited on top of the first one. This second gold layer fully covers the implanted area and ensures complete containment of the radiation emitted in the EC of ^{163}Ho. Ion implantation has been selected to enclose the ^{163}Ho in particle absorbers, since this process does not degrade the performance of detectors and allows the source atoms to be contained in a defined volume [24]. Two channels of the array, each equipped with just one sensor, are dedicated to measuring the temperature variations of the chip. The two pixels of these channels do not contain ^{163}Ho. In addition, for seven channels, only one of the two pixels contains ^{163}Ho to allow for *in situ* background determination. For the remaining 27 channels, both pixels contain ^{163}Ho. In the ECHo-1k experiment, two ECHo-1k chips have been used. The detectors in these chips are identical except for the material of the thin implantation layer, i.e., gold in one case (ECHo-1k-Au) and silver in the other case (ECHo-1k-Ag). The characterization of these two arrays has been discussed in [25]. Each MMC channel is individually read out using the two-stage dc–superconducting quantum interference device (SQUID) scheme [33,34]. The preamplified voltage signals from MMC channels are digitized using 16-bit 125 MS/s analog-to-digital converter boards with synchronized clocks. The data acquisition software allows for online fitting of each trace passing the constant fraction trigger algorithm, providing guidance for the offline analysis. The temperature variation of the calorimeter following the energy release in the particle absorber has a pulse shape with time constants defined by the thermal properties of the detector. The amplitude is, in first approximation, directly proportional to the deposited energy. The acquired voltage signal conserves the pulse shape and the fairly linear dependence of the amplitude on the deposited energy. For the ECHo-1k detectors, the nonlinearity has been evaluated to be below 0.5% at 2 keV, and it is corrected with a quadratic energy calibration [21,25].

In [35], the basic concept of the analysis of ECHo data has been discussed. A two-step data reduction has been developed to discriminate single ^{163}Ho events from triggered noise, pileup events, and events possibly related to cosmic muons or natural radioactivity. No meaningful energy dependence has been observed, which implies no expected spectral distortions. Details on data reduction are given in the Appendix. Figure 2 shows the measured ^{163}Ho spectrum along with the convolution between the theoretical model derived in [36] and the Gaussian detector response (solid line). The model, based on an *ab initio* approach, represents the most precise description of the electron capture process in ^{163}Ho but still fails in describing the tails and, therefore, cannot be used for fitting. The spectrum features about 200 million events between 100 and 5000 eV (blue part of the histogram in Fig. 2). The lower energy threshold is defined after correcting for trigger-level inhomogeneity among the channels. The effective energy resolution determined by the analysis of the MII line, expected to be described by only one resonance, is $\Delta E_{\rm FWHM} = 6.95(16)$ eV, obtained with a Voigt fit over the energy range 1824–1848 eV and with a Lorentzian width of 8.1 eV determined in a calibration measurement. This value is then used as input parameter in the fit of the end-point region. Other important parameters for the fit of the end-point region of the ^{163}Ho EC spectrum are the position and intrinsic width of the MI line, modeled in first approximation as a simple Lorentzian, $E_{\rm MI} = 2040.3(1)$ eV and $\Gamma_{\rm MI} = 14.0(2)$ eV. The unresolved pileup fraction $f_{\rm pu}$, which defines the intensity of the pileup background in the region of interest, is determined as the product of the activity per pixel and the rise time of the signal to be $f_{\rm pu} = 0.8(5) \times 10^{-6}$. The fit of the end-point region is then performed using a simplified analytical function for the measured decay rate:

$$\frac{dN}{dE} = C \times [A(E) \times F_{\rm PS}(E, Q)] \otimes g(E, \sigma) + b(E), \quad (1)$$

where C is a constant. $A(E)$ describes the atomic physics contribution to the differential electron capture decay rate. In [36], a theoretical prediction of the differential electron capture nuclear decay rate is given. In the end-point region, $A(E)$ is mainly determined by the $3s$ electron capture followed by an Auger decay slightly modified by the sum over all possible decay channels and their interferences [19]. The Auger matrix elements are energy dependent, leading to a roughly Lorentzian line shape at the resonance and an exponential decay in the high-energy tail [36].

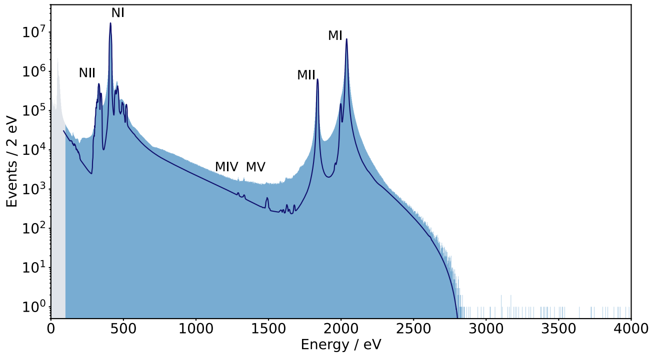

FIG. 2. Calorimetrically measured ^{163}Ho EC spectrum in the ECHo-1k experiment consisting of about 200 million events. The solid line is the output of a theoretical model [36] convoluted with a Gaussian having $\sigma = 2.8$ eV.

$F_{\mathrm{PS}}(E, Q)$ represents the part of the phase space function, which depends on the Q value and on m_{ν_e}: $F_{\mathrm{PS}}(E, Q) = (Q - E) \times \sqrt{(Q - E)^2 - m_{\nu_e}^2}$. The term in squared brackets in Eq. (1) is then convoluted with the Gaussian detector response $g(E, \sigma)$ with standard deviation σ determined by fitting the MII line. $b(E)$ is the background, which is composed of two contributions $b(E) = b_{\mathrm{const}} + b_{\mathrm{pu}}$. b_{const} is an energy-independent contribution due to natural radioactivity, which is in agreement with the expectation in [37,38]. b_{pu} represents the unresolved pileup contribution given by the normalized autoconvolution of the experimental spectrum weighted by the total number of acquired ^{163}Ho events N_{tot} and the unresolved pileup fraction f_{pu}: $b_{\mathrm{pu}} = N_{\mathrm{tot}} \times f_{\mathrm{pu}} \times (dN/dE \otimes dN/dE)$. The parameters b_{const} and f_{pu} have been determined by fitting the data in the energy region [2900, 5000] eV, where only 80 events are present. For the present analysis, an analytical approximation for the function describing the atomic physics contribution needed to be defined. Two analytical functions are used for approximating $A(E)$. As discussed in [36], the function describing the atomic physics contribution is varying very slowly in the end-point region. Thus, $A(E)$ can be approximated to a high level of accuracy by a simple exponential function in a small energy window below the end point. The first analytical function has, therefore, the form $A_1(E) = k_{\mathrm{exp}} \times e^{-E/\lambda}$. The parameters k_{exp} and λ are determined in a grid fit of the spectrum in the range 2450–2750 eV using Eq. (1) for a massless neutrino, Gaussian detector response, constant background, and $Q = 2863.2$ eV [17]. In the second approach, the fitting range is increased toward smaller energies to reduce the statistical error on the fit parameters. The high-energy tail of the MI resonance, which dominates the spectral intensity in the end-point region, is very complex. A simple Lorentzian, S_{MI}, roughly describes the region around the maximum, whereby the tail shows, both experimentally and theoretically, clear deviations from a Lorentzian line shape. The approach used in [15] is followed, and the deviation from a simple Lorentzian shape is described by adding a second function, S_{B}, which is responsible for increasing the intensity of the spectrum toward the end-point region:

$$A_2(E) = k_{\mathrm{MI}} \times \frac{\frac{\Gamma_{\mathrm{MI}}}{2\pi}}{(E - E_{\mathrm{MI}})^2 + \frac{\Gamma_{\mathrm{MI}}^2}{4}} + k_{\mathrm{B}} \times \Theta(E - E_{\mathrm{B}}) \times (-e^{-(E-E_{\mathrm{B}})/E_1} + e^{-(E-E_{\mathrm{B}})/E_2}). \quad (2)$$

The constants k_{MI} and k_{B} indicate the intensity of the two contributions. E_{B} is the characteristic energy at which the additional contribution becomes important, while E_1 and E_2 are the energy scales on which the two exponential functions vary. The parameters describing $A_2(E)$ are first searched with a grid fit over the energy range 2250–2750 eV assuming massless neutrinos, fixed position, and intrinsic width of the Lorentzian, fixed standard deviation for the Gaussian detector response, constant background, and unresolved pileup fraction as well as $Q = 2863.2$ eV [17]. The parameters describing the two $A(E)$ functions as derived with the grid fits are used to perform a Bayesian inference on the histogram of the end-point region of the ^{163}Ho EC spectrum. The aim is to simultaneously estimate posterior distributions of the

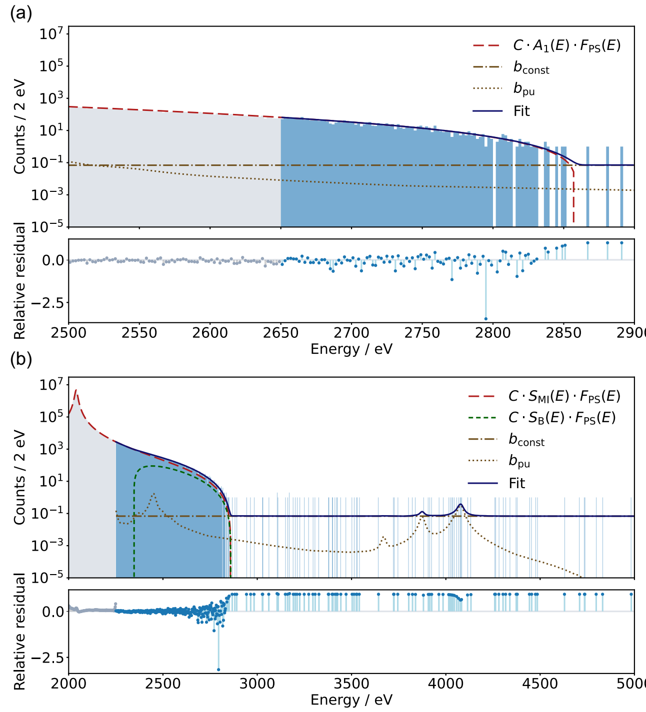

FIG. 3. Histogram of the end-point region with superimposed fit function (blue solid line) with A_1 (a) and A_2 (b). For both plots, the fitting region is indicated with the blue histogram. The two brown lines, dotted and dash-dotted, represent the two background contributions b_{pu} and b_{const}, respectively. The dashed lines represent the atomic physics functions multiplied with F_{PS}.

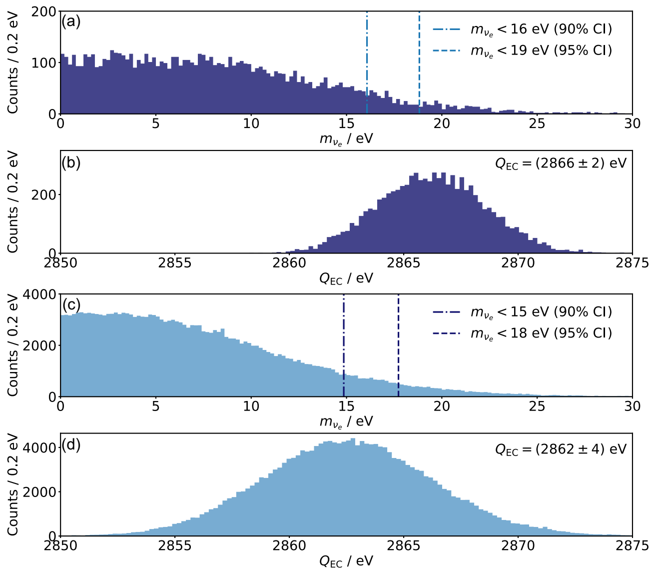

FIG. 4. Posterior distribution for Q and m_{ν_e} calculated for A_1 [(a) and (b), respectively] and for A_2 [(c) and (d), respectively].

spectral shape parameters, Q value, and neutrino mass to best explain the data under the assumption of Poisson statistics. Using the Stan statistical software platform [39], this estimation was accomplished through the Hamiltonian Monte Carlo algorithm, specifically using the implementation of the No-U-Turn sampler. The parameters describing the ^{163}Ho EC spectrum and the constant background are included with a normal prior, while for the effective neutrino mass a flat prior for $0\ \text{eV} < m_{\nu_e} < 100\ \text{eV}$ is used. Noninformative priors are used in case of A_2, while for A_1 all priors, besides the effective neutrino mass, need to be constrained to the grid uncertainties due to a large correlation among them. This is due to the presently relatively small number of counts in the fit region.

Figure 3(a) shows the histogram of the end-point region of the ^{163}Ho EC spectrum with the fit function for A_1 as a blue solid line (fitting range 2650–2900 eV, blue part of the histogram). The red dashed line represents $C \times A_1 \times F_{\text{PS}}$. Figure 3(b) shows the histogram in a larger range with the fit function for A_2 as a blue solid line (fitting range 2250–5000 eV, blue part of the histogram). The red dashed line represents the product of S_{MI} and F_{PS}, while the green short-dashed line represents the product of S_{B} and F_{PS}. The single-background components are shown in both plots (b_{const} brown dash-dotted line and b_{pu} brown dotted line). The constant background derived in both fits is the same: $0.073(8)/2$ eV, which, given an effective exposure of $4000\ \text{pixel} \times \text{day}$, leads to a background rate of $b_{\text{const}} = 9.1(1.3) \times 10^{-6}\ \text{eV/pixel/day}$. The posterior distributions for Q and m_{ν_e} are shown in Fig. 4 for A_1 [Figs. 4(a) and 4(b)] and A_2 [Figs. 4(c) and 4(d)]. The Q value derived from the posterior distribution for A_1 is $Q = 2866.3(2.0)$ eV (error related to the narrow prior), and the neutrino mass limit is $m_{\nu_e} < 19$ eV at 95% credible interval (CI) ($m_{\nu_e} < 16$ eV at 90% CI). The corresponding values for A_2 are $Q = 2862(4)$ eV and $m_{\nu_e} < 18$ eV at 95% CI ($m_{\nu_e} < 15$ eV at 90% CI). The results obtained using the two different models for the spectral shape are compatible; nevertheless, the use of narrow priors in case of A_1 makes the derivation of Q and m_{ν_e} dependent on the parametrization. This, in turn, indicates that the use of a simple exponential function at the present level of statistics is not appropriate. This approach might become important once the total number of counts is at least one order of magnitude higher.

We have presented the analysis of the ^{163}Ho EC spectrum acquired within the ECHo-1k experiment consisting of about 200 million events. Two analytical functions have been tested to describe the end-point region of the ^{163}Ho EC spectrum in the absence of a complete theoretical model, A_1 and A_2. At the present level of statistics, the simplified function A_1 does not properly represent the data. Using A_2, the Q value was derived to be $Q = 2862(4)$ eV, which is in excellent agreement with the one determined via Penning-trap mass spectrometry [17]. The upper limit of the effective electron neutrino mass could be reduced to $m_{\nu_e} < 15$ eV (90% CI). This limit is in agreement with the expectation given the available statistics and the achieved very low background rate of $b_{\text{const}} = 9.1(1.3) \times 10^{-6}\ \text{eV/pixel/day}$. This new upper limit represents an improvement of almost one order of magnitude with respect to the value in [26] and of almost a factor of 2 with respect to the recent limit in [15]. This result sets the basis for the next stage of the ECHo experiment, ECHo-LE (ECHo Large Experiment) via the demonstrated stability of the detector performance (energy resolution and calibration), the low background rate, and a solid analysis framework, for both data reduction and interpretation of the spectral shape, the already achieved performance for the multiplexed readout of MMC arrays [40,41], and the demonstrated possibility to increase the activity per pixel [42]. In this experiment, 20 000 high-energy resolution MMC detectors containing 10 Bq ^{163}Ho readout using the microwave SQUID multiplexing scheme and operated for more than two years will allow to reach a sensitivity to the effective electron neutrino mass below $1\ \text{eV}/c^2$. This new upper limit on the effective electron neutrino mass together with the results in [15] strengthen the role of the ^{163}Ho-based experiments ECHo and HOLMES for a model-independent determination of the neutrino mass scale. In turn, this paves the way for comparing the value of the effective electron neutrino and antineutrino mass from future large-scale experiments for CPT violation test.

We acknowledge funding and support by the Deutsche Forschungsgemeinschaft (DFG, German Research Foundation) Research Unit FOR2202 Neutrino Mass Determination by Electron Capture in ^{163}Ho, ECHo [funding under Grants No. HA 6108/2 (M. B. and M. W. H.), No. GA 2219/2 (A. B., D. B., C. E., L. G., F. M., and C. V.), No. EN 299/7 (C. E., S. K., and M. W.), No. EN299/8 (C. E.), BL 981/5 (K. B., S. E., R. X. S., and C. S.), and No. DU 1334/1 (C. E. D., H. D., and K. W.)]. F. M. and A. B. acknowledge the support by the Research Training Group HighRR funded by the DFG. M. W. H., K. B., S. E., P. F., and M. D. acknowledge the support by the DFG through SFB 1225 ISOQUANT Project-ID No. 273811115. M. N. acknowledges financial support by the Karlsruhe School for Elementary Particle and Astroparticle Physics: Science and Technology (KSETA). L. E. A. P., R. G., T. M., O. S., and M. W. acknowledge the financial support by Helmholtz Association. D. H. and A. R. acknowledge support by the European Microkelvin Platform (EMP). We acknowledge the support of the clean room team, the Electronics Workshop and the Mechanical Workshop at the Kirchhoff Institute at Heidelberg University, the nuclear chemistry and radiation protection team at the Department of Chemistry, and the TRIGA staff at Mainz University (N. Bittner, C. Gorges, C. Mokry, D. Renisch, J. Riemer, J. Runke, and L. Winkelmann). The authors gratefully acknowledge the data storage service SDS@hd supported by the Ministry of Science, Research and the Arts Baden-Württemberg (MWK) and the DFG through Grant No. INST 35/1503-1 FUGG.

Data availability—The data that support the findings of this article are not publicly available upon publication because it is not technically feasible and/or the cost of preparing, depositing, and hosting the data would be prohibitive within the terms of this research project. The data are available from the authors upon reasonable request.

[1] A. de Gouvêa, Neutrino mass models, Annu. Rev. Nucl. Part. Sci. **66**, 197 (2016).

[2] H. G. Escudero and K. N. Abazajian, Status of neutrino cosmology: Standard ΛCDM, extensions, and tensions, Phys. Rev. D **111**, 043520 (2025).

[3] J. Lesgourgues and S. Pastor, Neutrino mass from cosmology, Adv. High Energy Phys. **2012**, 608515 (2012).

[4] J.-Q. Jiang, W. Giarè, S. Gariazzo, M. G. Dainotti, E. Di Valentino, O. Mena, D. Pedrotti, S. Santos da Costa, and S. Vagnozzi, Neutrino cosmology after DESI: Tightest mass upper limits, preference for the normal ordering, and tension with terrestrial observations, J. Cosmol. Astropart. Phys. 01 (2025) 153.

[5] F. T. Avignone, III, S. R. Elliott, and J. Engel, Double beta decay, Majorana neutrinos, and neutrino mass, Rev. Mod. Phys. **80**, 481 (2008).

[6] M. Agostini, G. Benato, J. A. Detwiler, J. Menéndez, and F. Vissani, Toward the discovery of matter creation with neutrinoless $\beta\beta$ decay, Rev. Mod. Phys. **95**, 025002 (2023).

[7] J. A. Formaggio, A. L. C. de Gouvêa, and R. G. H. Robertson, Direct measurements of neutrino mass, Phys. Rep. **914**, 1 (2021).

[8] M. Aker *et al.* (KATRIN Collaboration), Katrin: Status and prospects for the neutrino mass and beyond, J. Phys. G **49**, 100501 (2022).

[9] A. A. Esfahani *et al.* (Project8 Collaboration), Determining the neutrino mass with cyclotron radiation emission spectroscopy—Project 8, J. Phys. G **44**, 054004 (2017).

[10] M. G. Betti *et al.* (PTOLEMY Collaboration), Neutrino physics with the PTOLEMY project: Active neutrino properties and the light sterile case, J. Cosmol. Astropart. Phys. 07 (2019) 047.

[11] A. A. Amad *et al.*, Determining absolute neutrino mass using quantum technologies, New J. Phys. **27**, 105006 (2025).

[12] L. Gastaldo *et al.* (ECHo Collaboration), The electron capture in ^{163}Ho experiment—ECHo, J. Low Temp. Phys. **176**, 876 (2014).

[13] B. Alpert *et al.* (HOLMES Collaboration), HOLMES—The electron capture decay of ^{163}Ho to measure the electron neutrino mass with sub-eV sensitivity, Eur. Phys. J. C **75**, 112 (2015).

[14] M. Aker *et al.* (KATRIN Collaboration), Direct neutrino-mass measurement based on 259 days of KATRIN data, Science **388**, 180 (2025).

[15] B. K. Alpert *et al.* (HOLMES Collaboration), Most stringent bound on electron neutrino mass obtained with a scalable low temperature microcalorimeter array, Phys. Rev. Lett. **135**, 141801 (2025).

[16] L. Gastaldo *et al.* (ECHo Collaboration), The electron capture in ^{163}Ho experiment—ECHo, Eur. Phys. J. Spec. Top. **226**, 1623 (2017).

[17] Ch. Schweiger *et al.*, Penning-trap measurement of the Q value of electron capture in ^{163}Ho for the determination of the electron neutrino mass, Nat. Phys. **226**, 921 (2024).

[18] A. De Rújula and M. Lusignoli, Calorimetric measurements of ^{163}holmium decay as tools to determine the electron neutrino mass, Phys. Lett. **118B**, 429 (1982).

[19] M. Braß, C. Enss, L. Gastaldo, R. J. Green, and M. W. Haverkort, *Ab initio* calculation of the calorimetric electron-capture spectrum of ^{163}Ho: Intra-atomic decay into bound states, Phys. Rev. C **97**, 054620 (2018).

[20] A. Fleischmann, C. Enss, and G. M. Seidel, Metallic magnetic calorimeters, *Cryogenic Particle Detection*, edited by C. Enss, Topics in Applied Physics Vol. 99 (Springer, Berlin, Heidelberg, 2005), p. 151, 10.1007/10933596_4.

[21] A. Fleischmann, L. Gastaldo, S. Kempf, A. Kirsch, A. Pabinger, C. Pies, J. Porst, P. Ranitzsch, S. Schäfer, F. v. Seggern, T. Wolf, C. Enss, and G. M. Seidel, Metallic magnetic calorimeters, AIP Conf. Proc. **1185**, 571 (2009).

[22] S. Kempf, A. Fleischmann, L. Gastaldo, and C. Enss, Physics and applications of metallic magnetic calorimeters, J. Low Temp. Phys. **193**, 365 (2018).

[23] M. Krantz, F. Toschi, B. Maier, G. Heine, C. Enss, and S. Kempf, Magnetic microcalorimeter with paramagnetic temperature sensors and integrated dc-SQUID readout for high resolution x-ray emission spectroscopy, Appl. Phys. Lett. **124**, 032601 (2024).

[24] L. Gastaldo, P.-O. Ranitzsch, F. von Seggern, J.-P. Porst, S. Schäfer, C. Pies, S. Kempf, T. Wolf, A. Fleischmann, C. Enss, A. Herlert, and K. Johnston, Characterization of low temperature metallic magnetic calorimeters having gold

absorbers with implanted ^{163}Ho ions, Nucl. Instrum. Methods Phys. Res., Sect. A **711**, 150 (2013).

[25] F. Mantegazzini, A. Barth, H. Dorrer, Ch. E. Düllmann, C. Enss, A. Fleischmann, R. Hammann, S. Kempf, T. Kieck, N. Kovac, C. Velte, M. Wegner, K. Wendt, T. Wickenhäuser, and L. Gastaldo, Metallic magnetic calorimeter arrays for the first phase of the ECHo experiment, Nucl. Instrum. Methods Phys. Res., Sect. A **1030**, 166406 (2022).

[26] C. Velte *et al.* (ECHo Collaboration), High-resolution and low-background ^{163}Ho spectrum: Interpretation of the resonance tails, Eur. Phys. J. C **79**, 1026 (2019).

[27] P. T. Springer, C. L. Bennett, and P. A. Baisden, Measurement of the neutrino mass using the inner bremsstrahlung emitted in the electron-capture decay of ^{163}Ho, Phys. Rev. A **35**, 679 (1987).

[28] F. Mantegazzini, S. Allgeier, A. Barth, C. Enss, A. Ferring-Siebert, A. Fleischmann, L. Gastaldo, R. Hammann, D. Hengstler, S. Kempf, D. Richter, D. Schulz, D. Unger, C. Velte, and M. Wegner, Multichannel read-out for arrays of metallic magnetic calorimeters, J. Instrum. **16**, P08003 (2021).

[29] H. Dorrer *et al.*, Production, isolation and characterization of radiochemically pure ^{163}Ho samples for the ECHo-project, Radiochim. Acta **106**, 535 (2018).

[30] T. Kieck, S. Biebricher, Ch. E. Düllmann, and K. Wendt, Optimization of a laser ion source for ^{163}Ho isotope separation, Rev. Sci. Instrum. **90**, 053304 (2019).

[31] T. Kieck, H. Dorrer, Ch. E. Düllmann, V. Gadelshin, F. Schneider, and K. Wendt, Highly efficient isotope separation and ion implantation of ^{163}Ho for the ECHo project, Nucl. Instrum. Methods Phys. Res., Sect. A **945**, 162602 (2019).

[32] L. Gamer, Ch. E. Düllmann, C. Enss, L. G. Andreas Fleischmann, C. Hassel, S. Kempf, T. Kieck, and K. Wendt, Simulation and optimization of the implantation of holmium atoms into metallic magnetic microcalorimeters for neutrino mass determination experiments, Nucl. Instrum. Methods Phys. Res., Sect. A **854**, 139 (2017).

[33] D. Drung and M. Mück, SQUID electronics, *The SQUID Handbook: Fundamentals and Technology of SQUIDs and SQUID Systems, I*, edited by J. Clarke and A. I. Braginski (Wiley-VCH Verlag GmbH & Co. KGaA, 2004), 10.1002/3527603646.ch4.

[34] D. Drung, C. Hinnrichs, and H.-J. Barthelmess, Low-noise ultra-high-speed dc SQUID readout electronics, Supercond. Sci. Technol. **19**, S235 (2006).

[35] R. Hammann, A. Barth, A. Fleischmann, D. Schulz, and L. Gastaldo, Data reduction for a calorimetrically measured ^{163}Ho-spectrum of the ECHo-1k experiment, Eur. Phys. J. C **19**, 963 (2021).

[36] M. Braß and M. W. Haverkort, *Ab initio* calculation of the electron capture spectrum of ^{163}Ho: Auger–Meitner decay into continuum states, New J. Phys. **22**, 093018 (2020).

[37] A. Göggelmann, J. Jochum, L. Gastaldo, C. Velte, and F. Mantegazzini, Study of muon-induced background in MMC detector arrays for the ECHo experiment, Eur. Phys. J. C **81**, 363 (2021).

[38] A. Göggelmann, J. Jochum, L. Gastaldo, F. Mantegazzini, A. Barth, and R. Hammann, Study of naturally occurring radionuclides in the ECHo set-up, Eur. Phys. J. C **82**, 139 (2022).

[39] S. D. Team, Stan reference manual, version 2.34.1, https://mc-stan.org (2024).

[40] D. Richter, L. Hoibl, T. Wolber, N. Karcher, A. Fleischmann, C. Enss, M. Weber, O. Sander, and S. Kempf, Flux ramp modulation based MHz frequency-division dc-SQUID multiplexer, Appl. Phys. Lett. **118**, 122601 (2021).

[41] M. Neidig, T. Muscheid, R. Gartmann, L. E. Ardila Perez, M. Wegner, O. Sander, and S. Kempf, Full-scale microwave SQUID multiplexer readout system for magnetic microcalorimeters, arXiv:2509.07671.

[42] M. Griedel, F. Mantegazzini, A. Barth, E. Bruer, W. Holzmann, R. Hammann, D. Hengstler, N. Kovac, C. Velte, T. Wickenhäuser, A. Fleischmann, C. Enss, L. Gastaldo, H. Dorrer, T. Kieck, N. Kneip, Ch. E. Düllmann, and K. Wendt, From ECHo-1k to ECHo-100k: Optimization of high-resolution metallic magnetic calorimeters with embedded ^{163}Ho for neutrino mass determination, J. Low Temp. Phys. **209**, 779 (2022).

[43] P. C.-O. Ranitzsch, C. Hassel, M. Wegner, D. Hengstler, S. Kempf, A. Fleischmann, C. Enss, L. Gastaldo, A. Herlert, and K. Johnston, Characterization of the ^{163}Ho electron capture spectrum: A step towards the electron neutrino mass determination, Phys. Rev. Lett. **119**, 122501 (2017).

[44] A. Faessler, L. Gastaldo, and F. Šimkovic, Electron capture in ^{163}Ho, overlap plus exchange corrections and neutrino mass, J. Phys. G **42**, 015108 (2014).

[45] R. G. H. Robertson, Examination of the calorimetric spectrum to determine the neutrino mass in low-energy electron capture decay, Phys. Rev. C **91**, 035504 (2015).

[46] A. Faessler and F. Šimkovic, Improved description of one- and two-hole excitations after electron capture in ^{163}Ho and the determination of the neutrino mass, Phys. Rev. C **91**, 045505 (2015).

[47] A. Faessler, C. Enss, L. Gastaldo, and F. Šimkovic, Determination of the neutrino mass by electron capture in ^{163}Ho and the role of the three-hole states in ^{163}Dy, Phys. Rev. C **91**, 064302 (2015).

[48] A. Faessler, L. Gastaldo, and F. Šimkovic, Neutrino mass, electron capture, and the shake-off contributions, Phys. Rev. C **95**, 045502 (2017).

[49] A. De Rujula and M. Lusignoli, The calorimetric spectrum of the electron-capture decay of ^{163}Ho. The spectral endpoint region, J. High Energy Phys. 05 (2016) 015.

End Matter

Appendix: Data processing—The first step, called the time-info filter (TIF), contains algorithms selecting events on the basis of the trigger time. The filters implemented in this step are the coincidence filter to eliminate events when more than one detector channel is triggered within the coincidence time, the hold-off filter to eliminate events which occur on the tail of a previous event within the same channel, and the burst filter, which eliminates events in one channel if the rate in a given time interval exceeds a threshold defined based on the ^{163}Ho activity in that channel. The fraction of triggered traces identified as bad events by the TIF is 24.9% for the pixels in ECHo-1k-Ag and 5% for the pixels in ECHo-1k-Au, in both cases dominated by small-amplitude electromagnetic noise, as caused by cellular phones [35]. The higher exclusion fraction for ECHo-1k-Ag pixels is due to suboptimal shielding of the readout cables. This large fraction of excluded events, in particular, through the burst filter, leads to a reduced effective exposure of about 4000 pixel × day.

In the second data reduction step, events surviving the TIF are analyzed to identify and discard events whose shape differs from the expected pulse shape, obtained as average of a large number of ^{163}Ho MI signals. For the analysis of ECHo-1k data, a template fit method has been selected, and the χ^2 of the trace fit is used to filter out events such as pileup and triggered noise not identified with the TIF. The χ^2 selection region is defined on the histogram of the χ^2 values as the $\pm 3\sigma$ region around the maximum, assuming Gaussian distribution. In order to identify the leakage of possible spurious events in the region of interest of the ^{163}Ho spectrum above 2.5 keV, the χ^2 histograms are analyzed for different low threshold energies. A leakage contribution well below the statistical uncertainty has been estimated for the end-point region. After the χ^2 filter, 4.3% and 5.9% of the data surviving the TIF are discarded for ECHo-1k-Ag and ECHo-1k-Au, respectively. The major part of the discarded events, about 50%, has an energy below 100 eV and represents either low-amplitude triggered noise or change of slope of the baseline due to slight temperature fluctuations of the substrate, inducing a trigger. The fraction of discarded events at higher energy is in agreement with the expected number of pileup events. To evaluate a possible energy dependence of the applied filters, the ratio between the number of events in the NI line and the number of events in the MI line was analyzed. Datasets having this ratio outside 5 times the standard deviation are discarded. The fraction of removed events with respect to the events surviving the χ^2 filter is 8% for the ECHo-1k-Ag data, corresponding to measurements in which the working point of the SQUID readout was not stable, while for ECHo-1k-Au data the fraction of removed events was less than 0.1%. Similarly, the ratio between the number of events in the MI line and the number of events in the region 2.5–2.9 keV was monitored. No events among those surviving all previous cuts were discarded.

After pulse selection, two steps are still necessary before obtaining the energy spectra for each pixel. The first one is a correction for amplitude variations due to temperature variations of the chip. This correction is obtained by correlating the amplitude of events in the MI line with the voltage output of the two temperature channels on the chip.

The second and final step is the energy calibration using the resonances present in the ^{163}Ho EC spectrum. Already with the very first MMCs with implanted ^{163}Ho, the ECHo Collaboration has pointed out that the shape of the ^{163}Ho spectrum is more complex than foreseen [43]. This observation motivated several works proposing models describing the EC in ^{163}Ho [19,36,44–49]. The theoretical calculations which best describe the observed spectral features are based on an *ab initio* approach [19,36]. For this reason, after the ECHo-1k data acquisition, a new calibration measurement was performed. In this experiment, a ^{55}Fe source was used for the calibration of the ^{163}Ho spectrum acquired with pixels in the ECHo-1k-Ag array featuring an energy resolution below 5 eV FWHM. The determination of the line position was performed with a symmetric Gaussian fit for the MII line and an asymmetric Gaussian fit for the NI and MI lines, to account for the multiplet nature of those lines. The positions of the ^{163}Ho lines obtained with respect to the quadratic calibration function based on the ^{55}Fe lines do not differ much from the value in [43]—MI 2040.67(11) eV, MII 1836.55(11) eV, and NI 411.81(8) eV—but are more accurate. The same fitting range to extract the position of the ^{163}Ho lines in the calibration analysis is then applied to each single spectrum, and a quadratic function is used for calibrating the data. The parameters of the quadratic function for each pixel do not appreciably vary over the measurement time. As control procedure for the robustness of the calibration, the position of the calibrated lines is compared to the expected positions. The average deviation for the position of the calibrated lines is around 0.01%.

The determination of the energy resolution in the calibrated spectra for each pixel and for each measurement is then performed. This is estimated from the width of the NI line. This line was chosen over the others despite its more complex line shape, because it has the highest number of events with respect to the other lines. The distribution of the energy resolution as FWHM has a Gaussian shape giving an average value of $\Delta E_{\mathrm{FWHM}} = 7.2(5)$ eV for pixels in the ECHo-1k-Ag and $\Delta E_{\mathrm{FWHM}} = 5.2(3)$ eV for pixels in the ECHo-1k-Au. The effect of having single spectra with different energy resolution composing the high-statistics ^{163}Ho EC spectrum on the derivation of the parameters describing the end-point region has been studied through Monte Carlo simulations assuming massless neutrinos. The fit of the end-point region, applying algorithms described in the main text, provided Q values in agreement with the one fixed for the simulation within the statistical uncertainty. This ensures that the systematic error induced by ignoring the slight differences in detector response of the used pixels is still smaller than the statistical error.